Mechanics of 3D rock block erodibility

George, M.F.

University of California, Berkeley, CA, USA

Sitar, N.

University of California, Berkeley, CA, USA

ABSTRACT: A program of experimental and analytical studies was carried out to investigate the influence of geologic structure on the erodibility of blocky rocks. Until this study, very little data existed regarding hydraulic loads on 3D blocks or regarding the mechanics of erodibility of 3D blocks beyond simple cubes or prisms. Proper understanding of the block scour processes is necessary to ensure the safe and reliable operation of key civil infrastructure, such as dams, bridges and water conveyance tunnels. This paper covers the experimental results and observations from physical hydraulic model experiments to determine 3D block erodibility. The results of the hydraulic modeling are used to develop a block theory framework for analysis of block erodibility.

1. INTRODUCTION

Scour processes play an important role in the evolution of natural rock landscapes as well as present a potential hazard to civil infrastructure such as dams, spillways, bridges and water conveyance tunnels (Fig. 1). Removal of individual blocks of rock is a primary mechanism by which scour can occur and, accordingly, proper understanding of block scour processes is necessary to ensure the safe and reliable operation of such structures. Evaluation of 3D block erodibility requires detailed knowledge regarding hydraulic loads applied to the block in both a spatial and temporal sense. Data of this nature, however, are extremely limited in current literature. Prior research has focused on simplified rectangular or cubic block shapes (e.g., Reinius, 1986, Bollaert, 2002, Frizell, 2007, Federspiel et al., 2011, Duarte, 2014). However, in general, 3D blocks present a variety of kinematic failure modes, e.g.,

lifting, sliding, and rotation (Goodman, 1995), and the influence of the kinematic failure mode on block erodibility has not been explored.

In that context, a set of flume experiments with different flow rates and block configurations was carried out as part of a comprehensive study of the hydraulics of 3D rock block scour. Detailed measurements and observations of dynamic block response were made to characterize scour mechanics and to better understand the implications for block erosion thresholds.

Values are presented in prototype scale unless otherwise noted.

Fig. 1. Removal of large rock blocks from unlined spillway at Wivenhoe Dam in Australia (Stratford et al., 2013). For scale, spillway width is approximately 90 m.

2. EXPERIMENTAL SETUP

Scaled physical hydraulic model tests were performed at the University of California's Richmond Field Station (RFS). Tests were conducted in a 28 m long x 0.85 m wide x 0.91 m deep flume with an overall grade of 1% (Fig. 2). A wooden ramp was constructed within the flume to locally steepen the channel slope at the downstream end and increase flow velocity. The downstream section contained a rotatable block mold that housed a removable tetrahedral "rock" block made of concrete? which was rotated in 15 deg. increments (ψ) with respect to the flow direction between $\psi = 0$ deg. and 180 deg. (Fig. 3). Block properties are provided in Table 1. The downstream channel grade was 20%, making an overall grade of 21% at the block location, which was held constant for all tests.

Fig. 2. Flume/ramp overview at RFS.

Nine flow rates, Q_1 to Q_9, were tested which yielded corresponding mean stream-wise flow velocities between approximately 6 m/s to 10 m/s (Table 2). Turbulence in the block region was generated through the installation of seven upstream baffle blocks (Fig. 4). Flow turbulence was characterized by the turbulence intensity (T_u) which is the ratio of the root mean square vertical flow velocity component (u'_z) to the mean stream-wise flow velocity component (u_x). For low and high turbulence conditions, T_u was approximately 2% and 7%, respectively (Table 2).

Table 1. Block properties (model scale).

Block #	1	2	3
Protrusion	4 mm	1.5 mm	Flush
Edge Type	Rounded	Rounded	Rounded
Weight	546.4 g	505.4 g	476.6 g
Volume	232 cm^3	224 cm^3	209.3 cm^3
Density	2.36 g/cm^3	2.26 g/cm^3	2.28 g/cm^3
Dimension 1	140.3 mm	138.7 mm	136.3 mm
Dimension 2	140.2 mm	138.9 mm	136.7 mm
Dimension 3	106.6 mm	103.7 mm	104.6 mm
Dimension 4	106.7 mm	104.4 mm	103.3 mm
Dimension 5	107.5 mm	104.0 mm	104.2 mm
Dimension 6	131.2 mm	130.0 mm	127.0 mm
Notes: Schematic for block dimensions			
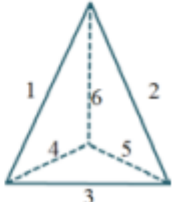
Table 2. Flow properties at block location.

Flow	Low T_u		High T_u	
	u_x (m/s)	T_u (%)	u_x (m/s)	T_u (%)
Q_1	2.33 (7.38)	-	2.08 (6.59)	-
Q_2	2.44 (7.70)	-	2.10 (6.65)	-
Q_3	2.51 (7.93)	-	2.22 (7.00)	-
Q_4	2.64 (8.35)	2.78%	2.38 (7.52)	6.61%
Q_5	2.71 (8.58)	2.48%	2.55 (8.07)	5.98%
Q_6	2.76 (8.72)	2.46%	2.59 (8.19)	6.25%
Q_7	2.84 (8.97)	2.21%	2.67 (8.45)	6.13%
Q_8	2.92 (9.23)	2.15%	2.70 (8.54)	6.95%
Q_9	2.96 (9.35)	2.17%	2.71 (8.57)	7.39%
Notes: u_x values in parenthesis are prototype scale velocity values determined using a model/prototype length scale ratio of 1/10 (Froude scaling).				

Block displacements were monitored using three proximity sensors (one per block mold face), while multiple pressure sensors (three per block mold face and one near each face on top of the block mold) were used to measure

hydraulic loads applied to block faces. Both displacement and pressure values were sampled at a frequency of 100 Hz (model scale). Additional information regarding the hydraulic model setup can be found in George (2015), George et al. (2015) and George & Sitar (2016).

3. RESULTS

Three distinctive modes of block response behavior were observed in the experiments:

• Mode 1 – gradual block displacement with consistent direction

• Mode 2 – gradual block displacement with variable direction

• Mode 3 – dynamic block displacement with variable direction

The block response was a function of kinematic constraints associated with the orientation of the block as well as flow conditions around the block. Typical experiments highlighting each block response are presented below.
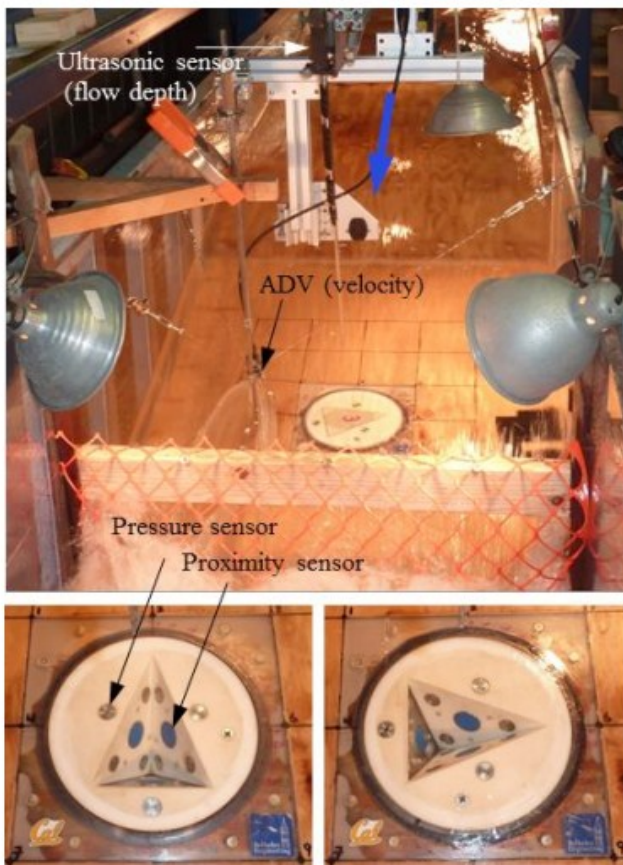

Fig. 3. Downstream ramp section showing block mold insert at angle of $\psi = 75$ deg. for low T_u flow conditions (top). Block mold at rotation angle $\psi = 0$ deg. (bottom left) and $\psi = 90$ deg. (bottom right).

3.1. Mode 1

Block orientations with a relatively low kinematic resistance to block movement in the downstream direction largely resulted in gradual displacement until removal, for both high and low T_u flow conditions. A "low" kinematic resistance refers to a block with a shallow dipping downstream face or shallow plunging line of intersection between two block faces such that the block can more easily slide in the downstream direction (Fig. 5).
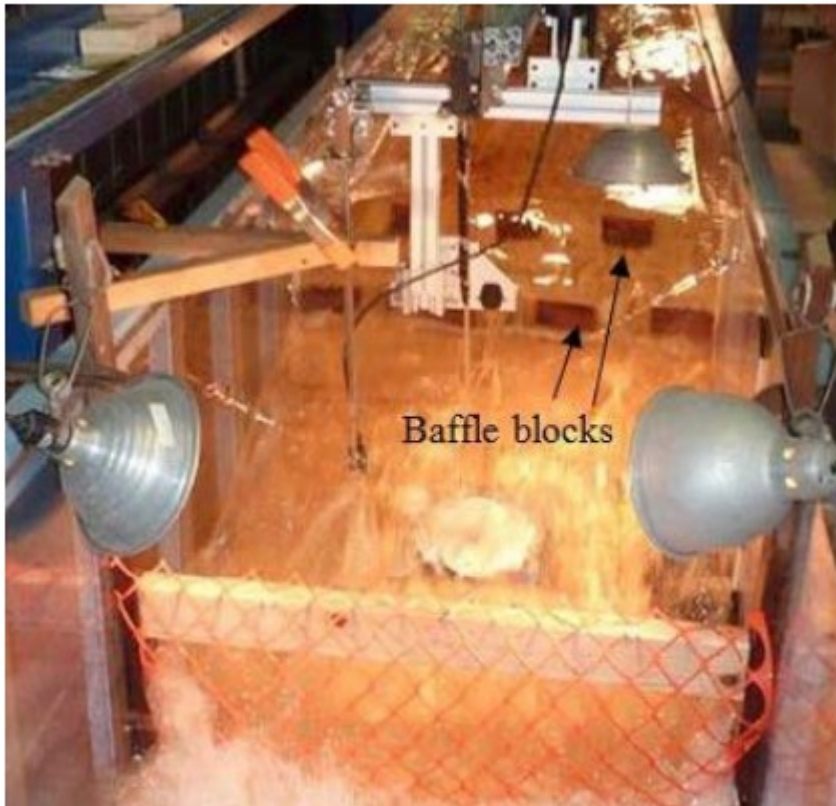

Fig. 4. High T_u flow conditions showing baffle blocks used to generate turbulence.

"Low" kinematic resistance

flow direction

block

shallow angle of downstream face or intersection of faces

"High" kinematic resistance

flow direction

block

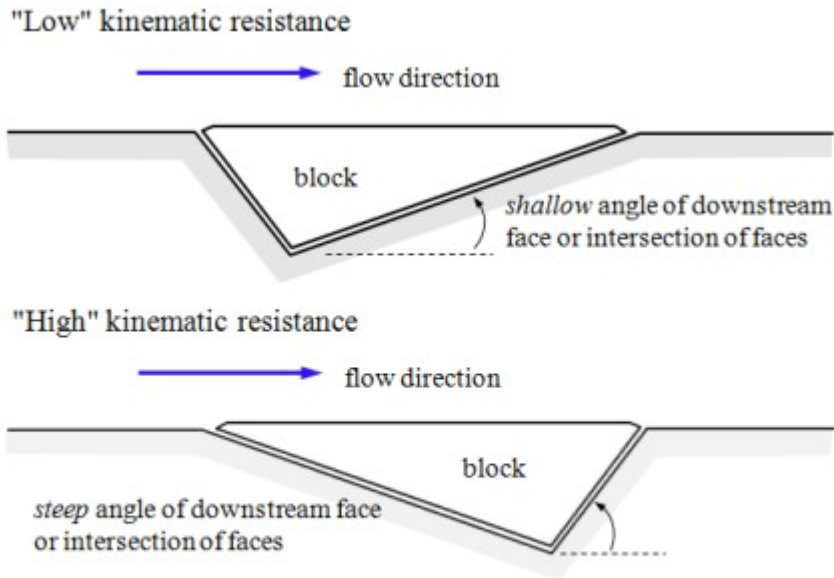*steep* angle of downstream face or intersection of faces

Fig. 5. Schematic of low (top) and high (bottom) kinematic resistance associated with block / block mold geometry with respect to the flow direction.

Fig. 6 shows total displacement time-series for one of the blocks (Block 2) from its original starting position under low T_u conditions for Q_4 discharge for ψ = 180 deg. As indicated, the migration of the block from its original position occured very gradually over a period of nearly 300 s with individual displacements occurring at a very small scale, O($\sim$0.001 mm). As the block became more exposed above the channel bottom, the rate of displacement increased until finally the block was removed. Spatial distribution of block position can be seen in Fig. 7. Initial block position was at the origin but, over the length of the run, moved directly downstream along the line of intersection between faces 1 and 2.
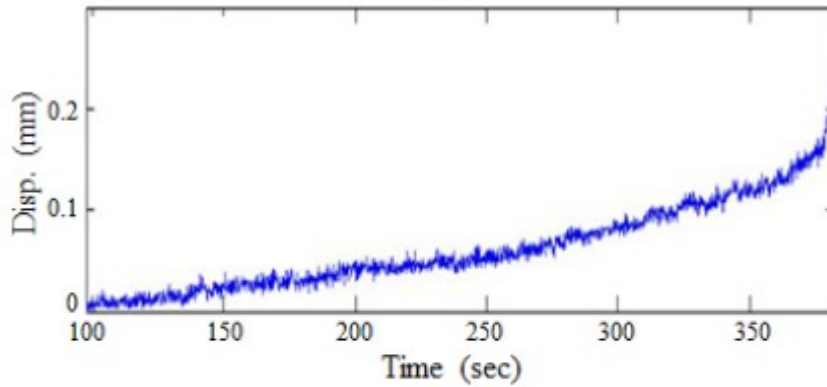
Fig. 6. Mode 1 – block displacement time-series showing gradual increase in total displacement magnitude until removal for $\psi = 180$ deg., low T_u, and Q_4.
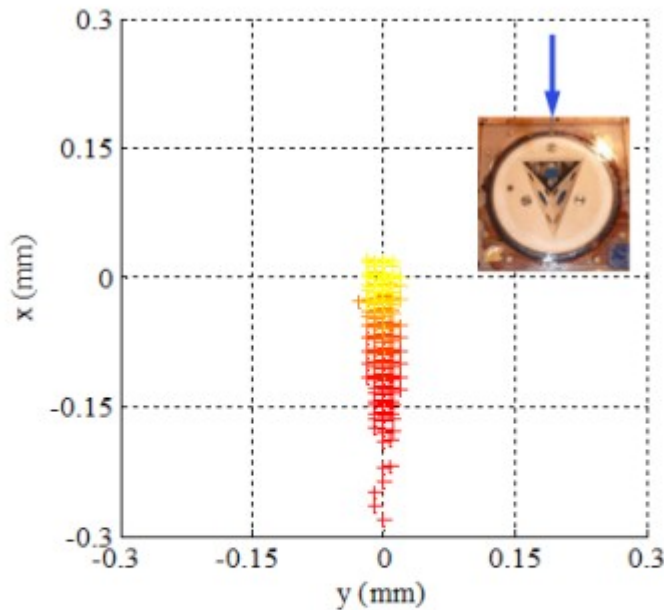

Fig. 7. Mode 1 – spatial distribution of instantaneous block position for $\psi = 180$ deg., low T_u, and Q_4 . Markers colored yellow to red with increasing time. Block movement along the line of intersection (i_{12}) of face 1 and face 2. Plot axes are swapped to correspond to flume coordinates.

A stereonet showing great circles corresponding to faces 1, 2 and 3 of the block, as well as the orientation of the instantaneous displacement vector (i.e., the vector from the initial to current block position), is presented in Fig. 8. Early displacement orientations (yellow markers) tended to be more random, while subsequent orientations (red markers) become more constrained in the upward direction along the intersection of faces 1 and 2,

denoted as $\mathbf{i}_{12}$. This indicates the kinematic mode of failure for Block 2 was 2-plane sliding on faces 1 and 2.
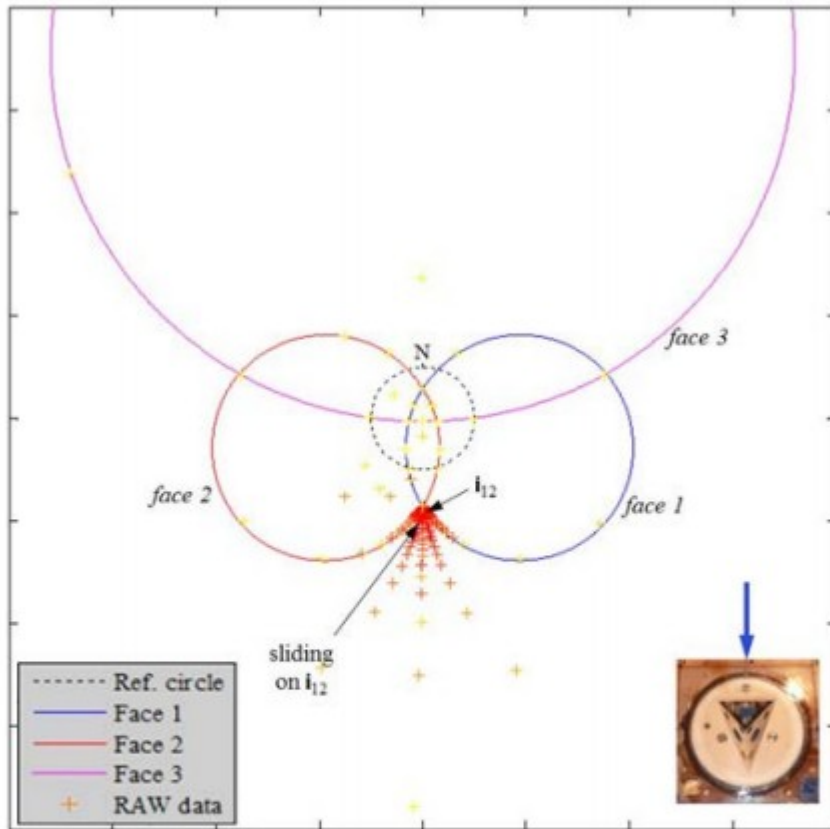

Fig. 8. Mode 1 – orientation of instantaneous vector from initial to current block position for $\psi = 180$ deg., low T_u, and Q_4. Markers colored yellow to red with increasing time. Predominant vector orientation at intersection of faces 1 and 2.

3.2. Mode 2

In orientations where block mold geometry yielded a higher kinematic resistance to erosion, block displacement was also gradual until removal (similar to mode 1 above). The direction of the block displacement, however, was considerably more variable.

Fig. 9 shows the block displacement with time for the case when $\psi = 30$ deg. Similar to Fig. 6, a gradual movement of the block was observed over a relatively long period of time (approximately 180 s). As the block was further exposed above the channel bottom, the rate of displacement increased until finally the block was removed. Individual block displacements were small and gradual without any large impulse-like movements.
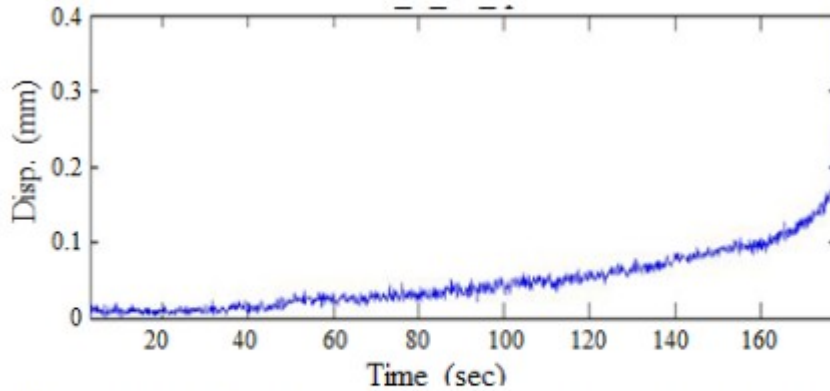
Fig. 9. Mode 2 – block displacement time-series showing gradual increase in total displacement magnitude until removal for ψ = 30 deg., low T_u, and Q_2.

The block (Fig. 10) initially moves slightly westnorthwest in the upstream direction into/along face 1. Then, as it lifts up, it starts moving downstream along the intersection of face 2 and 3 ($\mathbf{i}_{23}$) in a similar fashion to the case above, in which ψ = 180 deg. (Fig. 7 and Fig. 8) and sliding occurs along $\mathbf{i}_{12}$. The angle of intersection $\mathbf{i}_{23}$ is oriented 44 deg. above horizontal compared to $\mathbf{i}_{12}$ (for the case of ψ = 180 deg.) which is oriented 30 deg. above horizontal. The slope of the line of intersection between face 2 and 3 appears to provide enough added kinematic restraint to prevent the block from easily moving along $\mathbf{i}_{23}$ (Fig. 11). As indicated, the block follows a rather compound failure path leading up to block removal (red markers on the plot). This includes sliding on face 1, lifting, sliding on face 3 before lifting in direction of the azimuth of $\mathbf{i}_{23}$.
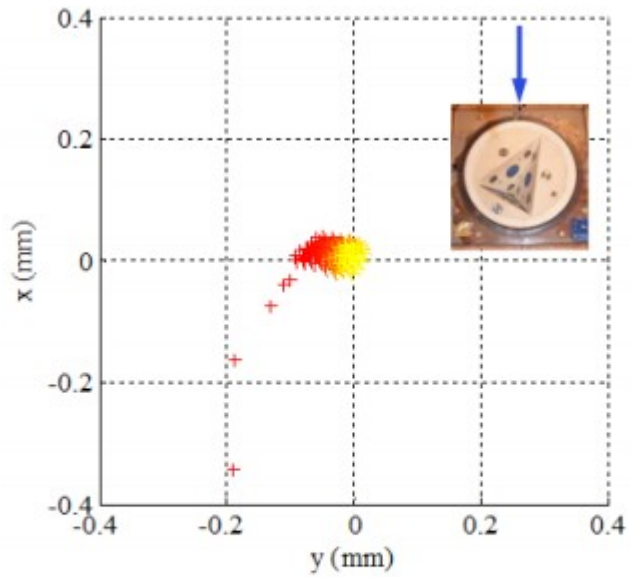
Fig. 10. Mode 2 – spatial distribution of instantaneous block position for ψ = 30 deg., low T_u, and Q_2. Markers colored yellow to red with increasing time. Note migration of block upstream to west-northwest prior to removal in southeast direction. Axes swapped to correspond to flume coordinates.
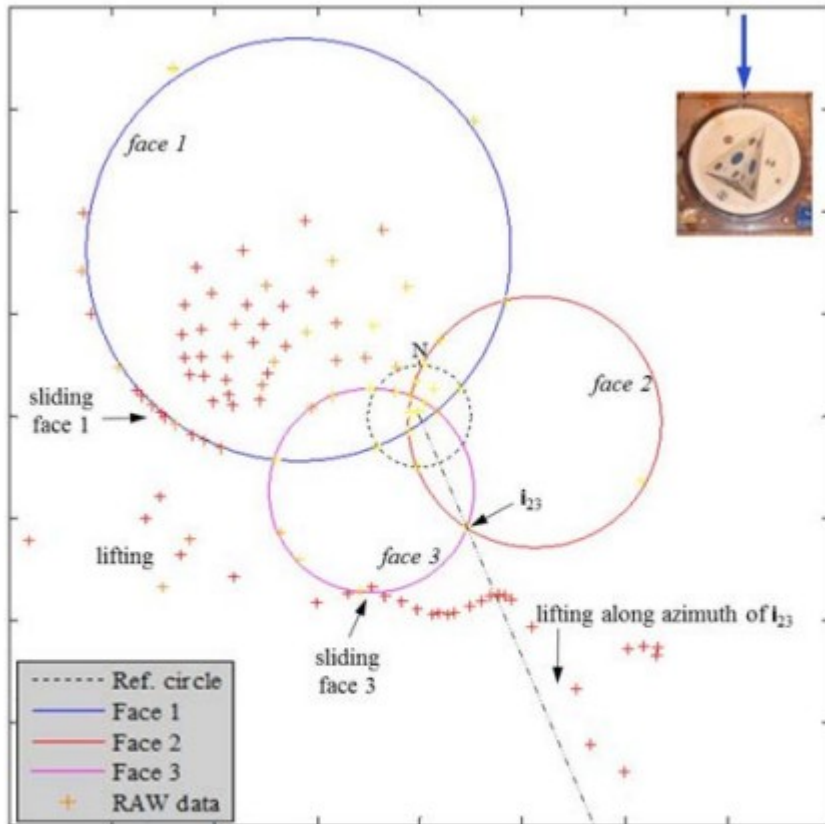
Fig. 11. Mode 2 – orientation of instantaneous vector from initial to current block position for ψ = 30 deg., low T_u, and Q_2. Markers colored yellow to red with increasing time. Note high variability in vector orientation.

3.3. Mode 3

For high T_u flow conditions and orientations where block mold geometry yielded higher kinematic resistance to erosion, block displacement response was significantly more dynamic in comparison with the previous two response types. Fig. 12 shows the block displacement time-series for the case when ψ = 0 deg. In contrast to mode 1 and 2 behaviors, the block movement occurred less frequently but with larger displacements responding to impulses applied to the block due to turbulence in the flow field. Four impulse events with displacements of approximately 0.2 mm to 0.6 mm are evident in the data, with the last impulse resulting in removal of the block. The duration of each impulse was approximately 0.1 s to 0.2 s.
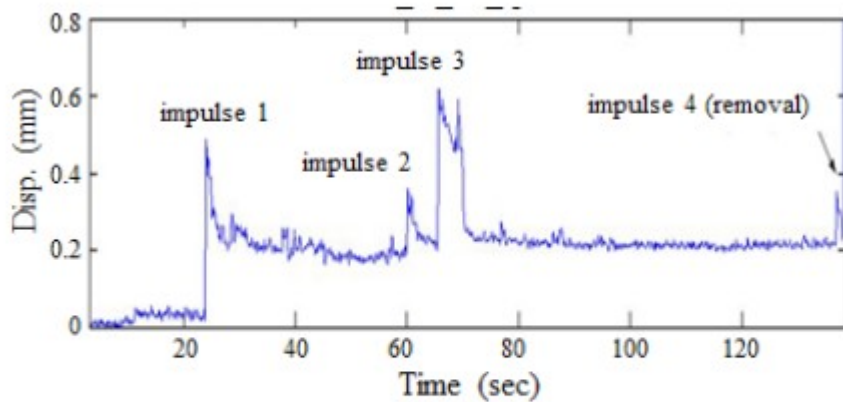
Fig. 12. Mode 3 – block displacement time-series showing larger displacements resulting from hydraulic impulses applied to the block for $\psi = 0$ deg., high T_u, and Q_7.

The instantaneous block positions are presented in Fig. 13. As shown in Fig. 14, block movements predominantly occurred by sliding on the downstream face of the block mold (face 3), but were highly variable in orientation. This can likely be attributed to the steep dip of face 3, which prevented easy sliding in the downstream direction.
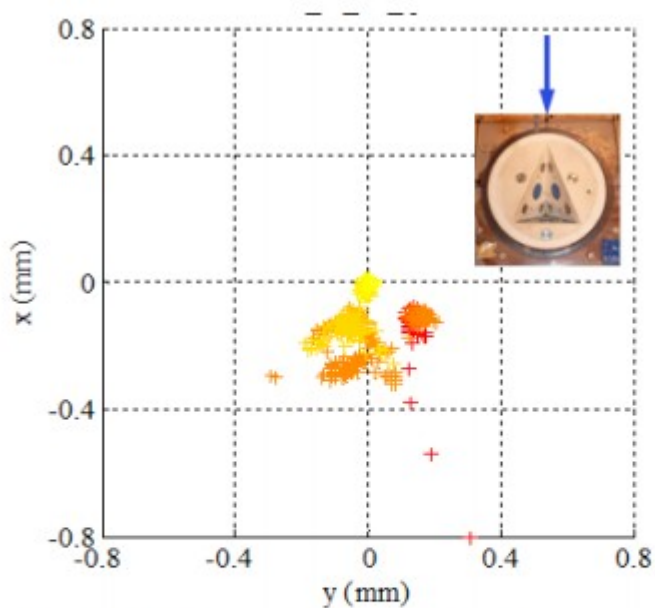

Fig. 13. Mode 3 – spatial distribution of instantaneous block position for $\psi = 0$ deg., high T_u, and Q_7. Markers colored yellow to red with increasing time. Note highly erratic block position. Plot axes are swapped to correspond to flume coordinates.
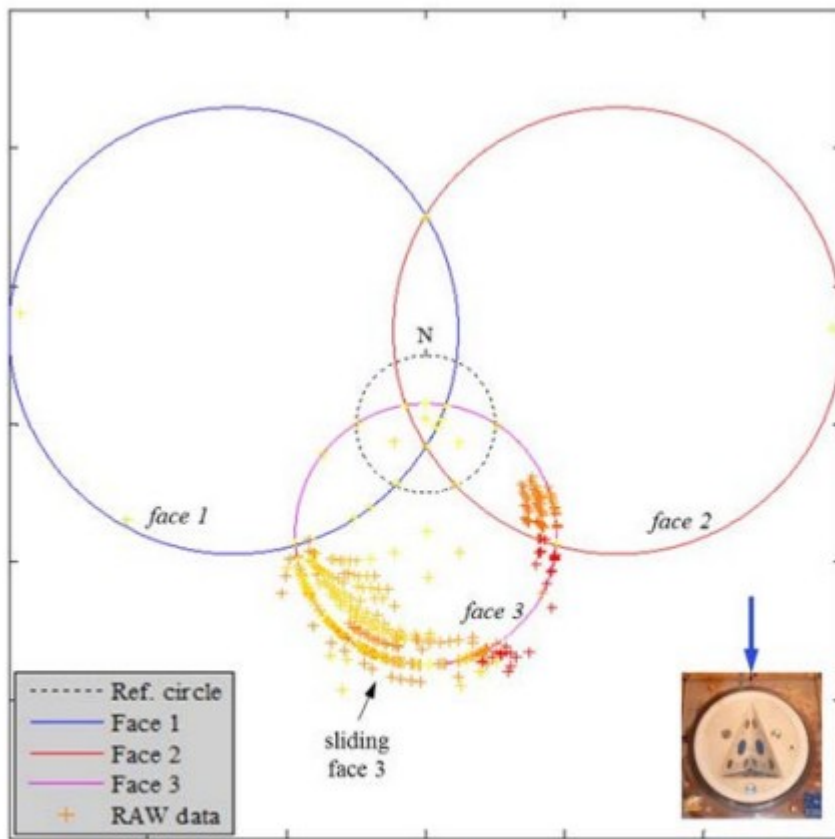
Fig. 14. Mode 3 – orientation of instantaneous vector from initial to current block position for $\psi = 0$ deg., high T_u, and Q_7. Markers colored yellow to red with increasing time. Predominant movement occurring along face 3.

Analysis of pressure and velocity data showed considerable fluctuations leading up to removal with a significant decrease in both occurring just prior to failure. Adapting a simplistic model from Hoffmans (2012), pressure and velocity measurements in the nearbed region were related to structure of turbulent eddies within the flow field. In this model, two (or more) oppositely rotating eddies, transported downstream at mean flow velocity, result in alternating high and low pressure zones near the channel bottom with localized areas of flow acceleration and deceleration. These regions were mapped alongside instantaneous velocity and displacement data (Fig. 15) and indicate a large zone of flow deceleration occurred prior to failure, which greatly decreased pressure in the vicinity of the block. The low pressure zone in the block region allowed flow from the next upstream eddy to accelerate towards the block, increasing pressure around the faces, causing the block to slide out from its mold. It appears that the low pressure zone on the channel bottom (face 4) may have been influential initiating block removal. The period of the eddy just prior to block removal was approximately 0.65 s, corresponding to a frequency of 1.5 Hz (4.9 Hz model scale). This is in near

agreement with the dominant frequency observed from spectral analysis of high T_u velocity data, which ranged from approximately 0.6 to 1.3 Hz (2 to 4 Hz model scale) due to the presence of the baffles (George, 2015).
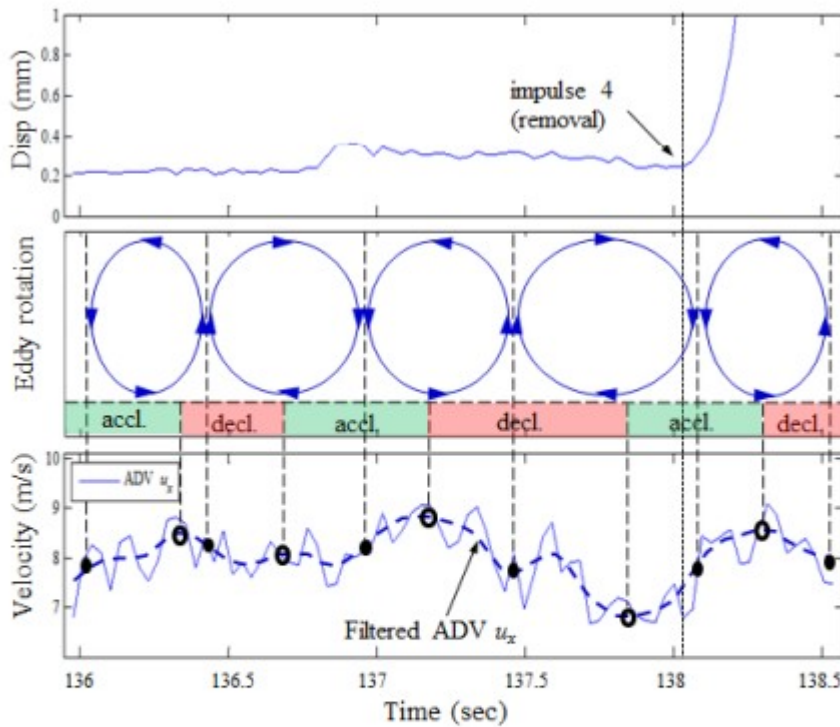

Fig. 15. Mode 3 – turbulent eddy structure associated with instantaneous values for displacement (top) and stream-wise flow velocity (bottom) for impulse 4 (Fig. 12) for $\psi = 0$ deg., high T_u, and Q_7. ADV time series data using a Butterworth low pass filter with cutoff frequency of 10 Hz is also shown.

Table 3 shows a summary of block response and failure modes for all model runs resulting in block removal. Block mode 1 behavior is observed when the block mold provides a low kinematic resistance in the downstream direction (i.e., $\psi \geq 135$ deg.). For values of $\psi < 135$ deg., mode 2 and mode 3 are generally witnessed as the kinematic resistance associated with the block mold orientation is higher. Mode 3 typically only occurs when the flow depths are large enough (associated with higher flow rates) such that eddies generated from the baffle blocks are large enough to cause impulse-type movements of the block.

3.4. Implications for block erodibility threshold

The block erodibility threshold as a function of kinematic constraints of the block mold and its relative orientation to flow direction is shown in (Fig. 16). The mean channel flow velocity resulting in removal of one of the tested blocks (Block 2) for high and low T_u flow conditions is presented as a function of block mold rotation angle. As can be seen, the block erodibility threshold

is highly dependent on the orientation of the block with respect to the flow direction.

Table 3. Block failure mode and response type by model run.

Run ID[a]	Failure Mode[b,c]	Resp.
000_H_b2_q7	S3	3
000_L_b1_q3	S1 (early), L/S3 (late)	2
000_L_b1_q3_2	S3 (early), L/S3 (late)	2
000b_H_b2_q7	Did not capture failure	3
000b_L_b1_q7	S3	2
000c_H_b1_q4	S2, S23, S3	2
000c_H_b2_q7	S3 (early), S2/S3 (late)	3
000c_L_b1_q7	S3	2
015_H_b1_q2	L (early), S2/S3 /L (late)	2
015_L_b1_q2	S12/S2 (early), S2/L (late)	2
030_H_b2_q3	S1 (early), S1/L/S3 (late)	2
030_L_b2_q2	S1 (early), S1/L/S3 (late)	2
045_H_b2_q2	S1/S3 (early), S1/L/S3 (late)	2
060_H_b2_q1	S1/S2 (early), L/S3 (late)	2
060_L_b2_q1b	S1/S2 (early), L/S2 (late)	2
090_H_b2_q1	S2/S3/S23 (early), L/S2 (late)	2
090_H_b2_q1a	S3 (early), L/S2 (late)	2
090_L_b2_q1	S2 (early), L/S2 (late)	1, 2
090b_H_b2_i3_q1	L (early), L/S2 (late)	1, 2
090c_H_b2_i2_q1	S2/S3/S23 (early), L/S2 (late)	2
105_H_b2_q3	S2 (early), L/S2 (late)	1,2
105_L_b2_q3	S2/S3/S23 (early), L/S2 (late)	2
120_H_b2_q4	S1/S2 (early), L/S2 (late)	3
135_H_b2_q5	S12/L	1,3
135_L_b2_q6a	S12	1
150_H_b2_q5	S12	1
150_L_b2_q8a	S12	1
150_L_b2_q9	S12	1
165_H_b2_q4	S2(early)/S12(later)	1
165_L_b2_q6	S12	1
180_H_b1_q1	S2/S12	1
180_L_b2_q4	S12	1
180b_H_b2_q3	S12	1
180c_H_b2_q3	S12	1

Notes:
[a] Mold rotation angle_Turbulence intensity_Block #_Flow Rate

[b] Based on displacement data plotted on stereonet
[c] L = lifting, S1 = sliding on face 1, S12 = sliding on face 1 & 2, etc.

Theoretical predictions for the block erodibility threshold are also presented in Fig. 16 using a block theory (Goodman & Shi, 1985) approach. The hydraulic forces for determination of the active resultant force vector (**r**) were estimated using best-fit data based on hydraulic model testing results (George & Sitar, 2016). For both high and low T_u flow conditions, the block theory approach appears to reasonably represent the erodibility threshold as determined by model tests. A block yield condition, corresponding to a joint friction angle, ϕ = 16 deg., was used based on dry and wet testing of the blocks sliding from the block mold. For block mold rotation angles, ψ < 135 deg., a better fit to the model data was achieved when a mobilized joint friction angle, ϕ = 0 deg. was used. This is related to the more dynamic response behavior observed for mode 2 and 3. It is hypothesized that the additional block movements associated with these modes, resulted in a decrease in the joint shear strength. Mode 2 and 3 are observed to occur when the required rotation angle (θ_r) of the active resultant force from its initial position to the limit equilibrium condition (see, e.g., Kieffer & Goodman, 2012 or George, 2015) is approximately 60 deg. This is related to the higher kinematic resistance afforded by the block mold geometry for these orientations.
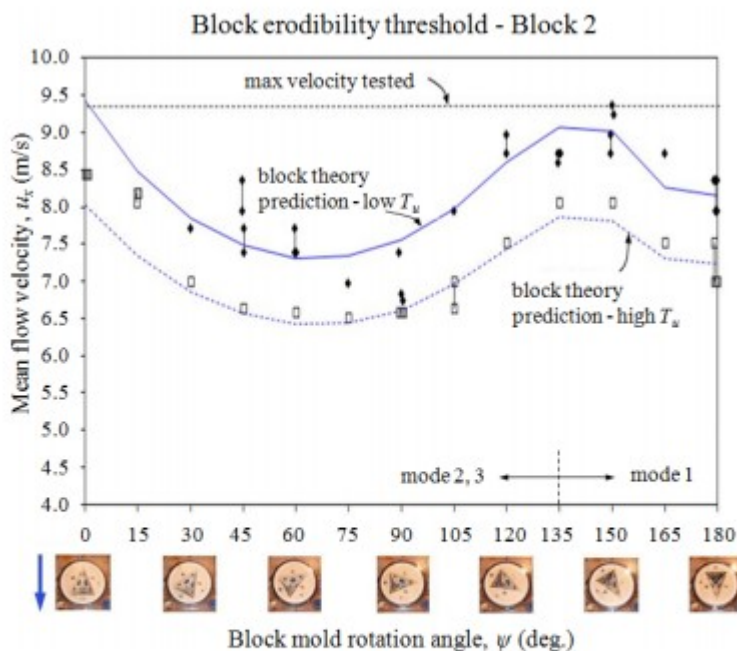

Fig.16. Prediction of block erodibility threshold for high and low T_u flow conditions compared to measured data for Block 2 using a mobilized friction angle, ϕ = 0 deg. for ψ < 135 deg. (corresponding to mode 2 and mode 3).

Increases in joint roughness and joint stiffness (both normal and tangential) would likely act to increase the block erodibility threshold. It should be noted, however, that in-situ stresses for blocks at the surface are often relieved such that stiffness effects would be minor. Additionally, reliability

analysis of block erodibility (George, 2015, George & Sitar, 2016) indicates joint shear strength is less influential compared to other system variables, such as block kinematics and water pressures on block faces and is, therefore, of secondary concern for analysis.

4. CONCLUSIONS

A series of hydraulic model flume experiments was conducted to evaluate 3D block erodibility for a variety of flow conditions. Three block response modes were observed that influenced the block erodibility threshold. Block response was associated with the block mold orientation with respect to the flow direction as well as flow conditions (i.e., high or low T_u). For different block mold orientations, the kinematic resistance afforded by the mold geometry varied. For mold rotation angles $\psi \geq 135$ deg., i.e. mold configurations with a shallow dipping downstream face or shallow plunging line of intersection between two faces such that the block could easily slide in the downstream direction (mode 1), this resistance was relatively low. For mold rotation angles $\psi < 135$ deg., the kinematic resistance was higher which resulted in increased difficulty in moving the block in the direction of flow. Accordingly a more dynamic block response was observed (mode 2 and 3). Theoretical predictions of the block erodibility threshold using a block theory approach shows reasonable agreement with model study results. For block configurations exhibiting mode 2 or 3 response, a mobilized joint friction angle was used to represent the block yield condition. In this study, modes 2 and 3 occurred when the required rotation angle of the active resultant force vector was greater than approximately 60 deg., although it is unclear if this threshold may be extrapolated to other block geometries.

Numerical simulation of the model experiments is currently being explored. A non-trivial obstacle is the simulation of fluid turbulence at the channel scale with concurrent simulation of fluid flow within the narrow jointing surrounding the block. Accurate numerical simulation of the block erodibility process would allow for analysis of a variety of block and flow configurations more readily than through physical model testing, although the latter provides essential invaluable insights into the rock scour process.

5. ACKNOWLEDGEMENTS

REFERENCES

Bollaert, E.F.R. 2002. Transient water pressures in joints and formation of rock scour due to high-velocity jet impact, Communication No. 13. Ph.D. Dissertation. Laboratory of Hydraulic Constructions. Ecole Polytechnique Federale de Lausanne, Switzerland.

Duarte, R.X.M. 2014. Influence of air entrainment on rock scour development and block stability in plunge pools, Communication No. 59. Ph.D. Dissertation. Laboratory of Hydraulic Constructions. Ecole Polytechnique Federale de Lausanne, Switzerland.

Federspiel, M.P.E.A., E.F.R. Bollaert, and A.J. Schleiss. 2011. Dynamic response of a rock block in a plunge pool due to asymmetrical impact of a high-velocity jet. Proc. of the 34th IAHR World Congress, Brisbane, Australia, 2404-2411.

Frizell, W. 2007. Uplift and crack flow resulting from high velocity discharges over open offset joints - laboratory studies, Report 12-2007. U.S. Dept. of the Interior - Bureau of Reclamation.

George, M.F. 2015. 3D block erodibility: Dynamics of waterrock interaction in rock scour. Ph.D. Dissertation. University of California, Berkeley.

George, M.F., and N. Sitar. 2016. Geotechnical Engineering Report No. UCB-GT/16/01: 3D block erodibility: Dynamics of water-rock interaction in rock scour. University of California, Berkeley.

George, M.F., N. Sitar, and L.S. Sklar. 2015. Experimental evaluation of rock erosion in spillway channels. Proc. of the 49th U.S. Rock Mechanics Symposium (ARMA), San Francisco, CA, June 28-July 1, Paper 700.

Goodman, R.E. 1995. Block theory and its application. Géotechnique, 45(3): 383-423.

Goodman, R.E. and G. Shi. 1985. Block theory and its application to rock engineering, Englewood Cliffs, NJ, Prentice Hall.

Kieffer, D.S. and Goodman, R.E. 2012. Assessing scour potential of unlined rock spillways with the Block Scour Spectrum / Beurteilung der Kolkbildung in nicht ausgekleideten Hochwasserentlastungen in Fels mittels des Block Scour Spectrums. Geomechanics and Tunnelling, 5(5): 527-536.

Reinius, E. 1986. Rock erosion. Water Power and Dam Construction, (June): 43-48.

Stratford, C.E., E.F.R. Bollaert, and E.J. Lesleighter. 2013. Plunge pool rock scour analysis techniques - Wivenhoe dam spillway, Australia. Proc. of HYDRO2013, Innsbruck, Austria, 1567-1608.